

Measurements of ocean surface turbulence and wave-turbulence interactions

FABRICE VERON¹, W. KENDALL MELVILLE², AND LUC LENAIN²

¹*College of Marine and Earth Studies, University of Delaware.*

²*Scripps Institution of Oceanography, University of California, San Diego*

Submitted, *Journal of Physical Oceanography*, XXXX-XXX-XX

February 19, 2008

Corresponding author address:

Fabrice Veron, 112C Robinson Hall. University of Delaware, College of Marine and Earth Studies,
Newark DE, 19716

E-mail: fveron@udel.edu

Report Documentation Page				Form Approved OMB No. 0704-0188	
Public reporting burden for the collection of information is estimated to average 1 hour per response, including the time for reviewing instructions, searching existing data sources, gathering and maintaining the data needed, and completing and reviewing the collection of information. Send comments regarding this burden estimate or any other aspect of this collection of information, including suggestions for reducing this burden, to Washington Headquarters Services, Directorate for Information Operations and Reports, 1215 Jefferson Davis Highway, Suite 1204, Arlington VA 22202-4302. Respondents should be aware that notwithstanding any other provision of law, no person shall be subject to a penalty for failing to comply with a collection of information if it does not display a currently valid OMB control number.					
1. REPORT DATE 19 FEB 2008		2. REPORT TYPE		3. DATES COVERED 00-00-2008 to 00-00-2008	
4. TITLE AND SUBTITLE Measurements of ocean surface turbulence and wave-turbulence interactions				5a. CONTRACT NUMBER	
				5b. GRANT NUMBER	
				5c. PROGRAM ELEMENT NUMBER	
6. AUTHOR(S)				5d. PROJECT NUMBER	
				5e. TASK NUMBER	
				5f. WORK UNIT NUMBER	
7. PERFORMING ORGANIZATION NAME(S) AND ADDRESS(ES) University of Delaware, College of Marine and Earth Studies, 112C Robinson Hall, Newark, DE, 19716				8. PERFORMING ORGANIZATION REPORT NUMBER	
9. SPONSORING/MONITORING AGENCY NAME(S) AND ADDRESS(ES)				10. SPONSOR/MONITOR'S ACRONYM(S)	
				11. SPONSOR/MONITOR'S REPORT NUMBER(S)	
12. DISTRIBUTION/AVAILABILITY STATEMENT Approved for public release; distribution unlimited					
13. SUPPLEMENTARY NOTES					
14. ABSTRACT The upper most layers of the ocean, along with the lower atmospheric boundary layer, play a crucial role in the air-sea fluxes of momentum, heat, and mass, thereby providing important boundary conditions for both the atmosphere and the oceans that control the evolution of weather and climate. In particular, the fluxes of heat and gas rely on exchange processes through the molecular layers, which are usually located within the viscous layer, which is in turn modulated by the waves and the turbulence at the free surface. The understanding of the multiple interactions between, molecular layers, viscous layers, waves and turbulence is therefore paramount to an adequate parameterization of these fluxes. In this paper, the authors present evidence of a clear coupling between the surface waves and the surface turbulence. When averaged over time scales longer than the wave period, this coupling yields a spatial relationship between surface temperature, divergence and vorticity fields that is consistent with spatial patterns of Langmuir turbulence. The resulting surface velocity field is hyperbolic suggesting that significant stretching takes place in the surface layers. On time scales for which the surface wave field is resolved, we show that the surface turbulence is modulated by the waves in a manner qualitatively consistent with rapid distortion theory.					
15. SUBJECT TERMS					
16. SECURITY CLASSIFICATION OF:			17. LIMITATION OF ABSTRACT Same as Report (SAR)	18. NUMBER OF PAGES 42	19a. NAME OF RESPONSIBLE PERSON
a. REPORT unclassified	b. ABSTRACT unclassified	c. THIS PAGE unclassified			

ABSTRACT

The upper most layers of the ocean, along with the lower atmospheric boundary layer, play a crucial role in the air-sea fluxes of momentum, heat, and mass, thereby providing important boundary conditions for both the atmosphere and the oceans that control the evolution of weather and climate. In particular, the fluxes of heat and gas rely on exchange processes through the molecular layers, which are usually located within the viscous layer, which is in turn modulated by the waves and the turbulence at the free surface. The understanding of the multiple interactions between, molecular layers, viscous layers, waves and turbulence is therefore paramount to an adequate parameterization of these fluxes. In this paper, the authors present evidence of a clear coupling between the surface waves and the surface turbulence. When averaged over time scales longer than the wave period, this coupling yields a spatial relationship between surface temperature, divergence and vorticity fields that is consistent with spatial patterns of Langmuir turbulence. The resulting surface velocity field is hyperbolic suggesting that significant stretching takes place in the surface layers. On time scales for which the surface wave field is resolved, we show that the surface turbulence is modulated by the waves in a manner qualitatively consistent with rapid distortion theory.

1. Introduction

The upper most layers of the ocean, along with the lower atmospheric boundary layer, play a crucial role in the air-sea fluxes of momentum, heat, and mass, thereby providing important boundary conditions for both the atmosphere and the oceans that control the evolution of weather and climate.

The first models of boundary layers on both sides of the air-sea interface were developed from our understanding of the turbulent flow over rigid flat surfaces and extended to the field after the landmark Kansas experiment on the terrestrial boundary layer (Businger et al., 1971). Consequently, models of neutrally stratified flows are based on the well-known “law of the wall” which depends on the assumptions of a constant stress layer and horizontal homogeneity. The velocity profile then depends on the stress, the vertical distance from the boundary, and the roughness length, z_0 , which parameterizes the influence of the roughness elements at the surface on the kinematics and dynamics of the flow. When the flow is stratified, “law of the wall” similarity theory is further modified to include buoyancy effects, which are parameterized by the so called Monin-Obukhov length, the height at which buoyancy and shear production of turbulence are of equal magnitude.

The air-sea interface, however, is dynamically quite different from a solid flat surface. For one thing, the velocity field is not required to vanish at the interface. The ocean surface responds with drift currents, surface waves and turbulent eddies over a broad range of scales. There are other phenomena such as bubble injection, spray ejection, rainfall, foam and surfactants, which further affect the dynamics and complicate the problem. Consequently, one would expect the dynamics of such an interfacial layer to be significantly different from that over a solid flat surface under similar

forcing conditions. Indeed, while there is evidence that, in general, and on average, the Monin-Obukov similarity theory holds over the ocean (Edson and Fairall, 1998; Edson et al., 2004), there are also some notable differences. Over the last decade or so it has also become apparent that surface wave processes can play an important role in the kinematics and dynamics of the boundary layers (e.g. Janssen, 1989, 1999; Komen et al., 1994; Belcher and Hunt, 1998; Hristov et al., 1998; Edson and Fairall, 1998, Uz et al., 2002; Sullivan et al., 2004, 2007), and recent measurements and models of the drag of the sea surface on the atmosphere at moderate to high wind speeds in fact suggest that much of the momentum transfer at the surface is supported by the form drag of the waves. There is also evidence that the air-sea heat flux can be modulated by the wavy surface (Sullivan and McWilliams, 2002; Veron et al., 2008a). In addition, breaking waves generate turbulence (Rapp and Melville, 1990; Agrawal et al., 1992; Thorpe, 1993; Melville, 1994; Anis and Moum, 1995; Melville, 1996; Terray et al., 1996; Veron and Melville, 1999a), which along with small scale Langmuir circulations and coherent structures (Melville et al., 1998; Veron and Melville, 1999b; McWilliams et al., 1997; Veron and Melville, 2001; Sullivan et al., 2004, 2007) may lead to enhanced dissipation and mixing with significant departures from the “law of the wall” and may also result in increased heat and gas transfer (Jähne et al., 1987; Hasse, 1990; Jähne and Haußecker, 1998; Zappa et al., 2001; Garbe et al., 2004; Schimpf et al., 2004; Turney et al., 2005).

With such richness in the phenomena and dynamics at the surface, one can also expect significant interactions between currents, surface waves, and turbulence. A well known example is Langmuir circulation that results from the interactions between vorticity and the Stokes drift generated by the surface waves (Leibovich, 1983; Thorpe 2004). On smaller time scales, there is also evidence that the turbulence can be significantly coupled with the surface waves (Lumley

and Terray, 1983; Cheung and Street, 1988a, 1988b; Thais and Magnaudet, 1995; Teixeira and Belcher, 2002).

Since the air-sea transfers of heat and gas rely in part on exchanges through the diffusive surface layers, and since these layers are typically smaller than the viscous sub-layer, our ability to adequately quantify these fluxes depends on our understanding of the small-scale turbulence that controls the dynamics of the molecular layers¹. In turn, our understanding of the small scale turbulence depends on our understanding of the multiple interactions between the turbulence, currents, and surface waves.

In this paper, we present results from field experiments that show evidence of coupling between the surface temperature, the surface turbulent velocity fields, and the surface waves. We also show evidence of coupling between the surface waves and the turbulent fields. In section 2, we summarize the experimental setup. In section 3, we present measurements of surface waves and the velocity fields which provide the basis for the results presented here. Section 4 shows the coupling of the waves with the surface kinematic fields and surface temperature over long time scales, when the wave effects are averaged in a manner similar to that which leads to the Craik-Leibovich mechanism (CLII) for the formation of Langmuir circulation (Leibovich 1983). Finally, section 5 shows evidence of distortion of the surface turbulence by the waves over short times scale when the wave field is resolved.

2. Experiments

The measurements described here were obtained from a field experiment conducted from *R/P*

¹In the case of gas transfer, these molecular layers can also be at the surface of entrained bubbles.

FLIP, moored approximately 150 miles off the coast of southern California, west of Tanner Bank ($32^{\circ} 40.20' N$, $119^{\circ} 19.46' W$, 300 m depth), during 20-26 August 2003.

The main instruments comprised an integrated active and passive infrared imaging and altimetry system (Veron et al., 2008b), and an eddy covariance atmospheric flux package. Both systems are described in more detail below.

a. Infrared imaging and altimetry system

The active and passive infrared imaging and altimetry system includes an infrared camera (Amber Gallileo), a 60 W air-cooled CO_2 laser (Synrad Firestar T60) equipped with an industrial marking head (Synrad FH index) with two computer-controlled galvanometers, a laser altimeter (Riegl LD90-3100-EHS), a video camera (Pulnix TM-9701), a 6 degree-of-freedom motion package (Watson Gyro E604), and a single board computer (PC Pentium 4). All instruments were enclosed in a weatherproof, air-conditioned, aluminum housing. All instruments and computers were synchronized together to within 2 ms and also to GPS time. The infrared camera was set to record temperature images (256×256 pixels) at 60 Hz, with a 2 ms integration time, yielding better than 15 mK resolution. The footprint of the infrared camera was approximately 2 m by 2 m. The video camera (768×484 pixels) was synchronized to the infrared camera and acquired full frames at 30 Hz. The foot print of the infrared camera was contained within the foot print of the video camera. The infrared CO_2 laser and accompanying marking head were used to actively lay down patterns of thermal markers on the ocean surface in order to study the rate of decay of an imposed surface temperature perturbation while tracking the Lagrangian velocity, shear, and vorticity at the surface. Finally, the laser altimeter measured the distance to the water surface at

12 kHz (averaged down to 50 Hz) with a foot print of 5 cm diameter, contained within both the infrared and video images. The system, among other things, yields the velocity at the surface by tracking active thermal markers laid down with the CO_2 laser (Thermal Marking Velocimetry, TMV) or by performing cross-correlation analysis on the passive surface temperature fields (Particle Image Velocimetry, PIV). The detailed performance of the passive and active IR measurement system for ocean-surface kinematics is described in Veron et al., 2008b.

FIG. 1

b. Eddy covariance system

In addition to the optical infrared system, we used an eddy covariance system to acquire supporting meteorological and atmospheric boundary layer flux data. The eddy covariance system included a three-axis anemometer/thermometer (Campbell CSAT 3), an open path infrared hygrometer/ CO_2 sensor (Licor 7500), a relative humidity/temperature sensor (Vaisala HMP45), and a net radiometer (CNR1). Turbulent fluxes of momentum, heat and moisture were calculated using the covariance method over 30-min averages. The sonic temperature was corrected for humidity and pressure, Rotation angles for correcting the orientation of the anemometer were obtained from the 30-min averages of the velocity components, and the latent heat flux was corrected for density variations (Webb et al., 1980). For the purposes of this paper, the good agreement between the flux covariance data and estimates using the Toga Coare 3.0 algorithm (Fairall et al., 1996; Fairall et al., 2003) supports the use of the Monin-Obukhov similarity theory for these open ocean conditions (Edson et al., 2004) and gave us confidence that our covariance measurements were adequate measurements of the total flux above the diffusive and wave boundary layers (see Veron et al., 2008b).

The instruments were deployed at the end of the port boom of *R/P FLIP* approximately 18 *m* from the hull at an elevation of 13 *m* above mean sea level (MSL).

The infrared optical system was set-up with the view ports clear of the end of the boom. The meteorological package was placed 15.5 *m* from the hull on the port boom with all instruments facing upwind with the exception of the net radiometer which was deployed with its axis downwind (figure 1).

We also deployed 2 fast response, high resolution, subsurface thermistors (RBR Ltd -1040 95 *ms* - 1 *Hz* sampling rate) placed at 1.2 *m* and 2 *m* from the mean sea level and fixed to the hull of *R/P FLIP*. An upward looking waves-enabled ADCP (RDI Workhorse 600kHz), was also rigidly mounted to *FLIP* at 15*m* depth and yielded directional wave spectra and significant wave height for the duration of the experiment. Finally, GPS position and *R/P FLIP* heading were sampled at 50 *Hz* and used to correct the ADCP data for *FLIP* motion and to align all other directions to true north.

The experiment described here took place from 20-26 August 2003. During this time, a 13.5 *s* swell was propagating towards $87^\circ \pm 17^\circ$. For the duration of the experiment the wind direction was relatively constant from $300^\circ \pm 12^\circ$. The wind speed however picked up from approximately 1 *m s*⁻¹ at the beginning of the week to 10 *m s*⁻¹ a few days later as a storm passed by (see figure 2a). Accordingly, a wind sea developed with waves of periods ranging from 1.7 *s* to 6.3 *s*, propagating towards $124^\circ \pm 12^\circ$. Finally, the surface currents were propagating towards $116^\circ \pm 21^\circ$ until 25 August 2003 at which point the current turned significantly. The keel of *FLIP* was facing $134^\circ \pm 4^\circ$ providing ideal conditions with wind, swell, surface currents, and wind-waves roughly aligned and with the study area, at and below the port boom, clear of *R/P FLIP*'s turbulent wake in both the air and the water.

3. Surface waves and velocity measurements

To examine the coupling between the surface temperature, the surface turbulent velocity fields and the surface waves, the surface wave elevation and direction of propagation must be measured. This was achieved here by single point laser altimetry measurements of the surface displacement combined with the direct measurements of the two-dimensional surface velocity over an area encompassing the single point altimetry data. Details are presented below.

a. Surface altimetry

The optical infrared system was equipped with a 12 kHz single point laser altimeter with a footprint on the surface of about 5 cm diameter at this operating height. It yielded instantaneous surface height η , at 50 Hz after averaging the raw 12 kHz data. The altimeter relies on the travel time measurement of a light pulse which reflects from the water surface. The altimeter performs significantly better when small scale surface roughness is present at higher wind speeds. For example, at 0.8 $m\ s^{-1}$ (8.4 $m\ s^{-1}$), 10 % (67 %) of the raw returns led to a valid height measurement. When necessary, dropouts were corrected by interpolating the height measurements using piecewise cubic Hermite polynomials. The footprint of the altimeter was situated 22 cm from the center of the infrared image. The altimeter data were used to measure wave parameters (figure 2) and the instantaneous distance from the imaging system to the ocean surface in order to calculate an instantaneous image resolution for the evaluation of the surface kinematics.

FIG. 2

Figure 2 shows the wind speed and direction along with the spectrogram of the surface elevation, and the significant wave height, for the duration of the experiment. The surface elevation spectrogram (Figure 2b) shows the swell peak at 15 – 20 s period and the wind-wave peak which

appears as the wind rises from 2 to 8 $m\ s^{-1}$, and exhibits a classical downshift in frequency as the wind-wave field grows. Figure 2c also shows good agreement between the significant wave height measured with the altimeter and that measured with the waves ADCP.

b. Surface Velocity

FIG. 3

We have shown that it is possible to calculate the two-dimensional surface velocity \mathbf{u} , and other kinematic variables from infrared surface temperature images (Veron et al., 2008b). The velocity at the surface can further be projected onto the directions parallel and perpendicular to the wind or wave directions. Here, we employ an algorithm typically employed for Particle Image Velocimetry (PIV) and calculate the surface velocity by performing a running normalized cross-correlation on sub-windows of surface temperature images separated by 33 ms . Each cross correlation yields a local average displacement (over the sub-window) which is then used in conjunction with the instantaneous image resolution and time interval between the successive images to estimate an average surface horizontal velocity. In most cases, we used 8x8 pixel sub-images with 50% linear overlap and image pairs separated by 166 ms yielding 6 velocity maps per seconds, each having with a spatial resolution of approximately 3 cm . Details on the performance of this technique can be found in Veron et al. (2008b). The surface velocity field \mathbf{u} obtained is the sum of velocities associated with the mean currents \mathbf{u}_c , the orbital velocity of the surface waves \mathbf{u}_w and the turbulence \mathbf{u}' . Figure 3 shows examples of the turbulent surface velocity field u'_i ($i = 1, 2$), obtained from the deviation from the image mean velocity, and calculated from an infrared surface temperature image taken under various wind speeds. The velocity fields are shown with the arrows and are overlaid on the first temperature image from which they were calculated. We show here

the turbulent velocity rather than the total velocity for easier visual comparison with the underlying temperature structures. The velocity field shows a variety of phenomena with vortices and regions of surface divergence and convergence that appear to be correlated with the surface temperature structure. For example, the region of warmer surface temperature in figure 3a appears to be associated with enhanced surface divergence.

The benefit of this PIV technique is the ability to simultaneously study processes involved in the evolution of the surface temperature and surface velocity fields including mean currents, wave orbital motions, and turbulence. In particular, direct surface velocity measurements, along with single point altimetry, allow us to measure surface wave directional spectra, and the spectra of the surface kinematics, as illustrated below.

c. Surface wave-directional spectra

For the scope of the work presented here, the single point altimetry from the laser altimeter and the surface velocity from the passive temperature images were combined to obtain the directional spectra of the surface wave field. Velocities at each corner of the infrared image were obtained by averaging all PIV estimates contained in local $30\text{ cm} \times 30\text{ cm}$ area. These four-corner velocities were then combined with the one point surface elevation measurements from the laser altimeter. Directional spectra were then computed using the WAFO toolbox (Wave Analysis for Fatigue and Oceanography, Lund University). The directional wave frequency spectrum can be associated to the cross spectrum between any two of the considered measured quantities, i.e. velocities and elevation (details can be found in Young 1994). To obtain estimates of the full directional spectrum, one must choose analysis methods capable of inverting the relation be-

tween those quantities. We considered two techniques, the Iterative Maximum Likelihood Method (IMLM, Pawka 1993), that corrects the directional spreading caused by the conventional MLM technique (Isobe et al., 1984, Capon, 1969), and the Maximum Entropy Method (MEM, Lygre and Krogstad 1986). Those two techniques showed some differences in the computed spectra, in particular in the spreading of the energy in the vicinity of the wave frequency peaks, but no significant direction differences at the wave energy peaks for swell and wind wave components. Wave peak directions and frequencies also show a good match with the ones obtained from a Hull-mounted RDI Wave ADCP. Only the peak frequencies and directions were used in the subsequent analysis.

4. Surface kinematics

In addition to measuring the velocity field at $O(1)$ cm spatial resolution we can also infer the velocity gradient tensor $\frac{\partial u_i}{\partial x_j}$ (Rafael et al., 1998). This gives the velocity gradient tensor with the same resolution and coverage as the velocity field. From there, one can infer all the two-dimensional first derivative kinematic fields including divergence D , vorticity ω , shear S , and normal deformation N :

$$2\frac{\partial u_i}{\partial x_j} = D \begin{pmatrix} 1 & 0 \\ 0 & 1 \end{pmatrix} + N \begin{pmatrix} 1 & 0 \\ 0 & -1 \end{pmatrix} + S \begin{pmatrix} 0 & 1 \\ 1 & 0 \end{pmatrix} + \omega \begin{pmatrix} 0 & -1 \\ 1 & 0 \end{pmatrix} \quad (1)$$

or alternatively,

$$D = \frac{\partial u_1}{\partial x_1} + \frac{\partial u_2}{\partial x_2}, \quad (2)$$

$$\omega = \frac{\partial u_2}{\partial x_1} - \frac{\partial u_1}{\partial x_2}, \quad (3)$$

$$S = \frac{\partial u_1}{\partial x_2} + \frac{\partial u_2}{\partial x_1}, \quad (4)$$

$$N = \frac{\partial u_1}{\partial x_1} - \frac{\partial u_2}{\partial x_2}, \quad (5)$$

Here, we examine the spatial distribution of the kinematics fields. Figure 4 shows the two-dimensional wavenumber spectra for the divergence and vorticity which were obtained from the PIV processing of the temperature images. Figure 4 also shows the two-dimensional wavenumber spectrum for the surface temperature. The spectra were obtained by averaging 120 individual spectra of a single velocity or temperature image, taken randomly during one minute of data. The data shown here were collected under wind speeds of 8 m s^{-1} at the beginning of the wind event at 05:03 UTC, on 23 Aug 2003, during the development of the wind sea. First, we note that the two dimensional spectra for the surface divergence, vorticity, and temperature, exhibit some anisotropy indicating that there is some degree of directionality in the structures of these spatial fields. Secondly, we note that the spectrum of the vorticity (4b) is approximately aligned with that of the temperature (4c). This is a consequence of the coupling between surface temperature and velocity. We know from previous work (Veron and Melville, 2001) that small scale Langmuir circulations and coherent turbulence (streaks) are present at these scales over this range of wind speeds. Even if instantaneous realizations of the surface temperature and velocity do not clearly exhibit such structures, time averages can reveal their presence. Here, the two-dimensional spectra are averaged over one minute of data. Colder streaks in the temperature images correspond to water parcels that have been organized by the underlying Langmuir cells and have collected in

FIG. 4

windrows at the surface. These water parcels have been in contact with the air the longest and therefore have had time to exchange significant heat, leading to colder surface temperatures. In addition, these parcels of water also have been exposed to the wind stress the longest and therefore, the “cold” surface temperature streaks also correspond to surface “jets” in which the surface velocity is larger than that of the surrounding fluid. This is illustrated in Leibovich (1983). As a consequence, there are two horizontal shear layers on each side of the temperature streaks where vertical vorticity is enhanced. Thus, when Langmuir circulations are present, the surface exhibits streaks of enhanced velocity, or surface jets, along with streaks of colder temperature and streaks of vorticity, all in the same direction and aligned with the wind. This is precisely what is shown in figure 4. The reader is reminded that the two-dimensional spectrum will show the largest signal in the direction of the largest variance, i.e. the direction perpendicular to the streaks. For example, in the data shown in figure 4, the vorticity (temperature) spectrum peaks at 52° (43°) indicating that the streaks in the vorticity fields are oriented along the direction $322^\circ - 142^\circ$ ($313^\circ - 133^\circ$), roughly aligned with the wind.

Finally, we note that the spectrum of the divergence is perpendicular to that of the vorticity. This is also consistent with the presence of Langmuir circulations. Indeed, Langmuir circulations are generated from the positive feedback between the surface jets, vertical vorticity, and the shearing and stretching of the vertical vortex lines by the Stokes drift (Craik 1977, Leibovich 1977). This means that the surface waves are propagating in the downwind direction, with their wavenumber vector approximately aligned in the direction of the surface streaks. Accordingly, regions of divergence and convergence associated with the non-linear surface wave field and even perhaps breaking waves, will be aligned parallel to the wave fronts, perpendicular to the jets of colder surface temperature and enhanced vertical vorticity. Indeed, for the data shown in figure 4,

the spectral peak for the divergence is approximately in the direction of the wind and wind waves indicating that the structure in the surface divergence field is perpendicular to the predominant wind and wind-wave directions, and also perpendicular to the streaks in the surface temperature and surface vorticity. Hence, when Langmuir circulations (or Langmuir turbulence) are present, the two-dimensional wavenumber spectra for the vorticity and divergence are perpendicular to one another with the spectrum for the vorticity parallel to that of the surface temperature. The presence of developing Langmuir circulations during the early stage of this wind event was also confirmed by visual inspection of the temperature images and visual observation of the surface during the experiment.

Before proceeding, it is useful to consider conditions and constraints on the surface velocity field that lead to orthogonality of the two-dimensional spectra of the divergence and vorticity as is observed in figure 4. Since the spectra shown in figure 4 were averaged over one minute of data, we start with the horizontal components of the mean surface velocity field defined by expanding the velocity about an arbitrary origin as follows:

$$u_i = u_{0i} + \alpha_i x_1 + \beta_i x_2 + \gamma_i x_1^2 + \delta_i x_2^2 + \chi_i x_1 x_2 + O(x_i^3), \quad (6)$$

where the u_i are approximated by quadratic functions of x_i , with cubic and higher terms neglected.

We can then estimate the divergence and vorticity respectively:

$$D = (\alpha_1 + \beta_2) + x_1(2\gamma_1 + \chi_2) + x_2(2\delta_2 + \chi_1) \quad (7)$$

$$\omega = (\alpha_2 - \beta_1) + x_1(2\gamma_2 - \chi_1) + x_2(\chi_2 - 2\delta_1) \quad (8)$$

$$(9)$$

When the two-dimensional spectra of the vorticity and divergence are orthogonal, the structures

(streaks in the case of Langmuir circulations) in the divergence and vorticity fields are also orthogonal. Consequently, the gradient on the velocity and divergence fields are orthogonal as well.

In other words,

$$\frac{\partial D}{\partial x_i} \frac{\partial \omega}{\partial x_i} = 0, \quad (10)$$

which leads to the following condition,

$$2(\gamma_1\gamma_2 - \delta_1\delta_2) - \chi_1(\gamma_1 + \delta_1) + \chi_2(\gamma_2 + \delta_2) = 0. \quad (11)$$

Providing that $\chi_i \neq 0$, this leads to:

$$\delta_i = -\gamma_i, \quad (12)$$

which in turns leads to a surface velocity field of the following hyperbolic form

$$u_i = u_{0i} + \alpha_i x_1 + \beta_i x_2 + \gamma_i(x_1^2 - x_2^2) + \chi_i x_1 x_2 + O(x_i^3), \quad (13)$$

We deduce here that when the surface velocity field is locally hyperbolic, which leads to significant stretching, then the two-dimensional wavenumber spectra for the vorticity and divergence are also orthogonal. Hyperbolicity is a sufficient condition for the spectra to be orthogonal, but it is not necessary. It is unclear whether or not the presence of Langmuir circulations leads to hyperbolic surface velocity fields and, to our knowledge, this question has not been examined. However, it is well established that Langmuir circulation will lead to significant stretching, and in particular stretching of vortex lines which incidentally leads to the positive feedback and reinforcement of the circulations. These data raise interesting questions about the nature of the surface velocity fields during periods of growing wind seas and developing Langmuir circulations.

In addition, the hyperbolic surface velocity field in equation 13 above immediately leads to $\frac{\partial S}{\partial x_i} \frac{\partial N}{\partial x_i} = 0$. That is, the two-dimensional wavenumber spectra for the shear and normal deformation are also orthogonal. While a hyperbolic velocity field is not a necessary condition for

this orthogonality, it is easy to demonstrate that $\frac{\partial D}{\partial x_i} \frac{\partial \omega}{\partial x_i} = 0$ implies $\frac{\partial S}{\partial x_i} \frac{\partial N}{\partial x_i} = 0$, and vice versa, consistent with the orthogonality of the shear and normal deformation fields shown here (Figure 5).

As the wind speed and wind wave field stabilize during 23 and 24 August 2003, we observe that the relationships between the two-dimensional spectra of the vorticity, divergence, shear and normal deformation show some additional order. Not only are the two-dimensional spectra perpendicular in pairs, that is the spectrum of vorticity (shear) is orthogonal to that of the divergence (normal deformation), but the spectrum for the vorticity (divergence) is orthogonal to that of the normal deformation (shear). This is clearly demonstrated in Figure 5 which shows the direction of the wind, waves and currents (a), along with the directions of the streaks (i.e. perpendicular to the direction of the peak spectral density) for the kinematic variables (Figure 5b). This further apparent coupling and ordering in the surface kinematics is presumably a consequence of the stabilization of the surface wind wave field and the wind drift. Using the simple formulation above for the velocity fields, this additional orthogonality yields a particular solution (though not the only one possible) with $\chi_i = \pm(-1)^i 2\gamma_i$ which indeed leads to a simpler, more constrained form of the local surface velocity fields

$$u_i = u_{0i} + \alpha_i x_1 + \beta_i x_2 + \gamma_i (x_1^2 - x_2^2) \pm (-1)^i 2\gamma_i x_1 x_2 + O(x_i^3). \quad (14)$$

FIG. 5

Figure 6 shows two examples of streamline patterns corresponding to a hyperbolic surface velocity field given by equation 14 where α_i , β_i , and γ_i where chosen randomly. The spatial scale is arbitrary. As expected, the hyperbolic surface velocity field shows some two-dimensional stretching and regions where the streamlines converge in a fashion that is reminiscent of the surface velocity field that one would expect in the presence of Langmuir circulations. In particular, figure

5b shows that the streamlines of the mean surface velocity converge to form surface streaks.

Later still during the week, on August 26 2003 and beyond, the geometric relationship between all kinematic fields is lost and no obvious coupling can be found (figure 5b). Unfortunately, the surface currents turned significantly during these two days (figure 5a). Consequently, it is difficult to unequivocally tie the apparent “loss of order” and the breakdown of the orthogonality between kinematics fields to either the drop in wind speed and the relaxation in the surface stress, which presumably destroyed the Langmuir circulations, or to the change in the direction of the surface currents, which at times, oppose the wave direction and Stokes drift.

Together, the data presented above illustrate that there are clear couplings that occur on time scales of a minute and longer which clearly appear out of long term spectral averages. The time average used here is similar to that used in the development of the CLII mechanism, and perhaps not surprisingly, the data shows that the surface kinematic fields are organized in a manner consistent with the presence of Langmuir circulations. These data highlight the need for further study of the relationship between the surface kinematics, surface waves, currents, and even perhaps the surface temperature and gas concentration (i.e. the surface molecular layer).

FIG. 6

5. Modulation of turbulence by the waves

We have seen in the preceding section that the surface kinematics is coupled with the developing wind seas, on time scales longer than approximately a minute. This raises the question of the coupling between the surface turbulence, waves, and currents on shorter time scales, and in particular the coupling between turbulence and surface waves.

As described above, the footprint of the laser altimeter was located within the infrared image

and therefore within the surface velocity and surface kinematic fields. This allows us to examine the modulation of the surface velocity and kinematic fields by the waves. From the infrared images and the resulting velocity images, along with the wave directional spectra obtained from the processing described in section 3.c, we have decomposed the surface velocity field into two components u_1 and u_2 , which, respectively, are aligned with, and orthogonal to, the direction of propagation of the wind-waves. To avoid sky reflectance and other effects in the infrared images, only night-time data were used. Also, as for the data shown in figure 3, we have subtracted image-mean velocity from every velocity vector of that particular PIV estimate. This operation subtracts both currents \mathbf{u}_c and wave orbital velocity \mathbf{u}_w , and yields the surface turbulent velocity field, \mathbf{u}' . From these we can generate time series of the statistics of the turbulent surface kinematics variables averaged over the footprint of the infrared imager.

For example, figure 7 shows time series of the variance of the turbulent surface velocity in the wave direction, $\overline{u_1'^2}$, and the surface displacement, η , over a 120s record starting at 05:00 (UTC) on August 24th, 2003. There is a clear visual correlation between the two variables with significant bursts of turbulence at the surface that correlate with the passage of surface waves. Also, high turbulent levels are located at, or slightly behind the wave crests. Spectral analysis makes this a little clearer.

Figure 8a shows frequency spectrograms of the surface displacement η for the duration of the *FLIP* experiment in August 2003. The quality of the near-IR laser altimeter data is dependent on the roughness of the sea surface with drop outs increasing for lower wind speeds. The data shown here were good for frequencies up to 1 Hz and are low-pass filtered at that frequency. The surface displacement spectra denoted by $S_{\eta\eta}$ is typical, showing both wind-wave and swell peaks. The wind-wave peak appears with the wind event (figure 2), showing the classical downshift in wind-

wave peak frequency with time. The spectra also show a f^{-4} slope above the wind-wave peak. Figure 8b shows that the frequency spectra for the turbulent velocity fluctuations in the direction of the wave propagation, u'_1 , exhibit peaks at the local maxima of the wind-wave spectra. Figures 8c and d show the squared coherence $C_{u'_1\eta}$ and phase $\Phi_{u'_1\eta}$, between u'_1 and η , respectively. It shows a peak in the squared coherence of approximately $0.2 - 0.3$, rapidly going to zero at frequencies above approximately 1 Hz . The phase between the turbulence and surface displacement near the peak of the coherence is slightly negative, indicating that the maximum in turbulence intensity lags the maximum surface displacement. This is presumably a consequence of the enhanced wind-stress and turbulence on the windward side of the wave. This is corroborated by identical results for the other kinematic variables (not shown). Incidentally, this is consistent with observations of warmer skin temperature also on the windward side of the waves that results from enhanced wind stress and the resulting turbulence which leads to the disruption of the aqueous viscous layer and the thermal molecular layer, i.e the cool skin (Simpson and Paulson, 1979; Miller and Street, 1978; Veron et al., 2008a).

Increased turbulence and vorticity near the wave peak could also be a result of the shearing effects on the turbulence and the local stretching of vortex lines by the passing surface waves (Teixeira and Belcher, 2002). We examine next the effect of the waves on the turbulence over short, wave resolved, time scales.

FIG. 7

FIG. 8

We wish to extract the wave-coherent turbulent quantities. Following the standard Reynolds decomposition $\mathbf{u} = \overline{\mathbf{u}} + \mathbf{u}'$ where the overbar represents spatial averages over the PIV estimates (which are distributed over the footprint of the infrared imager). The primes indicate fluctuating quantities taken as deviations from the mean which can be further decomposed into wave coherent, $\tilde{\mathbf{u}}$, and turbulent components, \mathbf{u}'' . Here we use a technique similar to that presented in Veron et

al., (2008a) to extract the averaged wave coherent quantities. We use the coherence and phase of each variable with the surface displacement, η , due to the waves. Denoting the spectrum of u'_1 by $S_{u'_1 u'_1}$, we find that the spectrum of u'_1 coherent with the waves (i.e. the spectrum of \tilde{u}_1) is given by $S_{\tilde{u}_1 \tilde{u}_1} = S_{u'_1 u'_1} \times C_{u'_1 \eta}$.

It follows that the variance of the phase-coherent velocity in the direction of the wave propagation, (\tilde{u}_1) , is given by:

$$\overline{\tilde{u}_1^2} = \int S_{\tilde{u}_1 \tilde{u}_1} d\omega, \quad (15)$$

FIG. 9

Figure 9 shows the variance of the wave-coherent, along wave, surface velocity turbulence as a function of the wind speed (a) and the surface wave slope² (b). While noisy, the data show that there is some fraction of the surface turbulence that is coherent with the surface waves. The data show that the variance of the wave coherent surface turbulence increases with wind speed and wave slope, with perhaps a tighter fit with the wave slope. Figure 9 also shows data taken in shallow water and at lower wind speeds from Scripps Pier during the winter of 2003 (see Veron et al., 2008b for details). The two data sets merge continuously and the large symbols are the bin averaged data. The solid lines show the linear fit through the data (forcing a zero intercept for figure 9b).

Of further interest is the total fraction of this wave coherent turbulence to the total turbulent intensities. Following the work of Townsend (1976, pp71-77) and Texiera and Belcher (2002), we use the frame work of rapid distortion estimate this ratio. Assuming initially isotropic turbu-

²Since the surface slope, (η_x, η_y) , was not directly measured in the experiments, the root mean square wave slope is instead approximated from the wave elevation frequency spectrum by $S = \left(\int_{0.5f_p}^{1.5f_p} S_{\eta\eta} k^2 df \right)^{\frac{1}{2}}$, where f_p is the peak frequency and k the wavenumber given by the dispersion relationship. Finally, we estimate $ak = \sqrt{2}S$. This is valid for the gravity wave range only.

lence and plane straining by a unidirectional, monochromatic linear wave field of amplitude a and wavenumber k , then

$$\frac{\overline{\tilde{u}_1^2}}{\overline{u_1'^2}} = -\frac{4}{5} \frac{(\beta - \beta^{-1})}{(\beta + \beta^{-1})} + \frac{3}{35} (\beta - \beta^{-1})^2 \quad (16)$$

where, β denotes the strain ratio, i.e. the ratio of the velocity gradient tensor (or vorticity components) with and without distortion. In this case, β varies as:

$$\beta \approx 1 - ak. \quad (17)$$

Neglecting terms higher than quadratic in the wave slope ak , we find that:

$$\frac{\overline{\tilde{u}_1^2}}{\overline{u_1'^2}} \sim \frac{4}{5} ak + \frac{26}{35} (ak)^2 \quad (18)$$

which indicates that the normalized wave-modulated turbulence in the direction of the wave propagation is of order $O(ak)$. It should be noted that this theoretical estimate relies on assumptions of isotropy and homogeneity in the turbulence. These can be violated near the surface (Belcher et al., 1994) and in the case where the turbulence is injected by localized breaking events; although, as noted by Texiera and Belcher (2002), even in the latter case, the integral length scale of the turbulence is small compared to the wavelength of the surface breaking wave, hence satisfying the scale separation necessary for rapid distortion theory to be applicable. On that note, we do not expect the swell to significantly affect the surface turbulence, at least in a rapid distortion sense, since the strain rate from the orbital motion of the swell is generally too weak compared to that of the turbulence on itself. In fact, figure 8c shows no coherence between the waves and the surface turbulence at the swell frequency. Finally, the estimate above is developed for monochromatic linear waves and not for a full wave spectrum, thus we expect differences between this idealized

theoretical prediction and the observed field data. Nevertheless, we feel that it is valuable and interesting to compare the data with the available theoretical estimates. Figure 10 shows the ratio of the variance of the wave coherent turbulence ($\overline{\tilde{u}_i^2}$) to the total variance in the turbulence ($\overline{u_i'^2}$) as a function of the rms wave slope. The variance ratio in the direction of the waves increases with the wave slope. We should note here that we expect this ratio to be relatively noisy, especially at low wind speeds and wave slopes as $\overline{u_i'^2}$ becomes smaller. In figure 10, we also show the theoretical estimate from equation 18. While there is a large scatter in the data, and an expected flattening due to noisy data for low surface wave slopes, the theoretical estimate agrees reasonably well with the data at the larger slopes. These data appear to be the first field observations qualitatively supporting the use of rapid distortion theory to predict the modulation of surface turbulence by surface waves.

FIG. 10

6. Conclusions

We have shown that there are periods of strong coupling between the surface wave field and wind forcing, and both the surface kinematic and temperature fields. During the early phase of the wind event described here, the two-dimensional wavenumber spectra of the surface vorticity and surface temperature, when averaged over time scales of one minute and longer show that these mean fields are organized in longitudinal structures aligned with the wind direction. In addition, we also show that the vorticity and divergence structures at the surface are orthogonal to each other. This coupling, which is revealed when the surface fields are averaged over many wave periods as is done with the CLII approach, is consistent with the presence of Langmuir circulations (or Langmuir turbulence). As the wind stabilizes, additional order in the surface kinematic

fields is found and the structures in the normal deformation and shear are aligned with that in the fields of surface divergence and vorticity, respectively. This orthogonality can be explained by a surface velocity field of hyperbolic form. In turn, hyperbolicity leads to significant stretching and convergence in the mean surface velocity field, once again consistent with the effects of Langmuir circulations.

Over short time scales where the waves are resolved, we observe the modulation of the surface turbulence by the surface waves. We show that there is a maximum wave-coherent turbulent intensity near the crests of the surface waves. These results are consistent with the modulation of the skin temperature by the surface waves where warmer temperatures, resulting presumably from the destruction of the molecular thermal layer by the turbulence, occur near the crest of the waves. Our data shows that the relative wave-coherent turbulent intensities vary with both wind speed and surface wave slope. The data are qualitatively consistent with rapid distortion theory but more work is needed for more complete quantitative comparisons.

Acknowledgements

We thank Peter Matusov for his help in the design, construction, testing and deployment of the original instrumentation. We thank the staff of the SIO Marine Development Shop for the fabrication of custom equipment. We thank Bill Gaines, Tom Golfinos and crew of the *R/P FLIP* for all their help in the field experiments, as well as John Hildebrand and Gerald D'Spain for sharing space and facilities onboard *R/P FLIP*. Finally we thank A.D. Kirwan for his suggestions regarding the surface kinematic fields. This research was supported by an NSF grant (OCE 01-18449) to WKM & FV and an ONR (Physical Oceanography) grant to WKM.

REFERENCES

- Agrawal, Y., Terray, E., Donelan, M., Hwang, P., Williams, A. J., III, Drennan, W. M., Kahma, K. K., & Kitaigorodskii, S. A. Enhanced dissipation of kinetic energy beneath surface waves. *Nature*, **359**: 219–220 (1992).
- Anis, A., & Moum, J. N. Surface wave-turbulence interactions: Scaling $\epsilon(z)$ near the sea surface. *J. Phys. Oceanog.*, **25**: 346–366 (1995).
- Belcher, S., Harris, J.A. & Street, R.L. Linear dynamics of wind waves in coupled turbulent airwater flow. Part 1. Theory. *J. Fluid Mech.*, **271**:119–151 (1994).
- Belcher, S., & Hunt, J. Turbulent flow over hills and waves. *Annu. Rev. Fluid Mech.*, **30**:507–538 (1998).
- Businger, J.A., Wyngaard, J.C., Izumi, Y., & Bradley, E.F. Flux-profile relationships in the atmospheric surface layer. *Journal Atmospheric Science.*, **28**:181–189 (1971).
- Capon, J. High resolution frequency-wavenumber spectrum analysis. *Proc. IEEE.*, **57**:1408–1418 (1969).
- Cheung, T.K. & Street, R.L. Turbulent layers in the water at an air-water interface. *J. Fluid Mech.*, **194**: 133-151 (1988a).
- Cheung, T.K. & Street, R.L. Wave-following measurement in the water beneath an air-water interface, *J. Geophys. Res.*, **93**(C11):14089-14097. (1988b)
- Craik, A.D.D. The generation of Langmuir circulations by an instability mechanism. *J. Fluid Mech.*, **81**: 209–223 (1977).
- Edson, J. B., & Fairall, C.W. Similarity relationships in the marine surface layer. *J. Atmos. Sci.*, **55**:2311–2328 (1998).

- Edson, J. B., Zappa, C.J., Ware, J.A., McGillis, W.R., & Hare, J.E. Scalar flux profile relationships over the open ocean. *J. Geophys. Res.*, **109**, C08S09, doi:10.1029/2003JC001960 (2004).
- Fairall, C. W., Bradley, E.F., Rogers, D.P., Edson, J.B., & Young, G.S. Bulk parameterization of air-sea fluxes for Tropical Ocean-Global Atmosphere Coupled-Ocean Atmosphere Response Experiment. *J. Geophys. Res.*, **101**, 3747–3764 (1996)
- Fairall, C.W., Bradley, E.F., Hare, J.E., Grachev A.A., & Edson, J.B. Bulk parameterization of air-sea fluxes: Updates and verification for the COARE algorithm. *J. Clim.*, **16**, 571–591 (2003)
- Garbe, C.S , Schimpf, U., & Jähne, B. A surface renewal model to analyze infrared image sequences of the ocean surface for the study of air-sea heat and gas exchange. *J. Geophys. Res.*, **109**(C8) doi 10.1029/2003JC001802 (2004).
- Hasse, L. On the mechanism of gas exchange at the air-sea interface. *Tellus*, **42B**: 250–253 (1990)
- Hristov, T., Friehe, C.A., & Miller, S. Wave coherent fields in the air flow over ocean waves: Identification of cooperative behavior buried in turbulence. *Phys. Rev. Lett.*, **81**:5245-5248 (1998).
- Isobe, M., Kondo, K. & Horikawa, K. Extension of MLM for estimating directional wave spectrum. Symposium on description and modelling of directional seas, DHI and MMI, Copenhagen, pp.1-15. (1984).
- Jähne, B., Munnich, K.O., Bosinger, R., Dutzi, A., Huber, W. & Libner, W. On the parameters influencing air-water gas exchange. *J. Geophys. Res.*, **92**: 1937–1949 (1987)
- Jähne, B. & Haußecker, H. Air water gas exchange. *Annu. Rev. Fluid Mech.*, **30**: 443–468 (1998).
- Janssen, P.A.E.M. Wind induced stress and the drag of air flow over sea waves. *J. Phys. Oceanog.*,

19:745–754 (1989).

Janssen, P.A.E.M. On the effect of ocean waves on the kinetic energy balance and consequences for the inertial dissipation technique. *J. Phys. Oceanogr.*, **29**:530–534 (1999).

Komen, G. J., Cavaleri, M., Donelan, M., Hasselmann, K., Hasselmann, S., & Janssen, P. *Dynamics and Modeling of Ocean Waves*. Cambridge University Press (1994).

Leibovich, S. On the evolution of the system of wind drift current and Langmuir circulations in the ocean. Part 1. Theory and average current. *J. Fluid Mech.*, **79**: 715–743 (1977).

Leibovich, S. The form and dynamics of Langmuir circulations. *Annu. Rev. Fluid Mech.*, **15**: 391–427 (1983).

Lumley, J. L., & Terray, E.A. Kinematics of turbulence convected by a random wave field. *J. Phys. Oceanogr.*, **13**: 20002007 (1983).

Lygre, A. & Krogstad, H.E. Maximum entropy estimation of the directional distribution in ocean wave spectra. *J. Phys. Oceanogr.*, **16**: 20522060 (1986).

McWilliams, J.C., Sullivan, P.P., & Moeng, C.-H. Langmuir turbulence in the ocean. *Journal of Fluid Mechanics.*, **334**, 1–30 (1997).

Melville, W. K. Energy Dissipation by Breaking Waves. *J. Phys. Oceanogr.*, **24**(10): 2041–2049 (1994).

Melville, W. K. The Role of Surface-Wave Breaking in Air-Sea Interaction. *Annu. Rev. Fluid Mech.*, **28**:279–321 (1996).

Melville, W. K., Shear, R., & Veron, F. Laboratory measurements of the generation and evolution of Langmuir circulations. *J. Fluid Mech.*, **364**: 31–58 (1998).

Miller Jr. A. W., & Street R.L. On the existence of temperature waves at a wavy air-water interface. *J. Geophys. Res.*, **83**(C3):1353–1365 (1978).

- Pawka, S.S. Island Shadow in Wave directional Spectra. *J. Geophys. Res.*, **88**:2579–2591 (1983).
- Rapp, R. J. Melville, W. K. Laboratory Measurements of Deep-Water Breaking Waves. *Phil. Trans. Roy. Soc. London.*, **A331**(1662): 735–800 (1990).
- Schimpf, U., Garbe, C., & Jahne, B. Investigation of transport processes across the sea surface microlayer by infrared imagery. *J. Geophys. Res.*, **109**(C8) doi:10.1029/2003JC001803 (2004).
- Simpson J.J., & Paulson C.A. Small-scale sea surface temperature structure. *J. Phys. Oceanog.*, **10**:399–410 (1980).
- Sullivan P.P., & McWilliams J.C. Turbulent flow over water waves in the presence of stratification. *Phys. Fluids*, **14**: 1182–1195 (2002).
- Sullivan P.P., McWilliams J.C., & Melville W.K. The oceanic boundary layer driven by wave breaking with stochastic variability. Part I: Direct numerical simulations, *J. Fluid Mech.*, **507**:143-174. (2004).
- Sullivan P.P., McWilliams J.C., & Melville W.K. Surface gravity wave effects in the oceanic boundary layer: large-eddy simulation with vortex force and stochastic breakers, *J. Fluid Mech.*, **593**:405–452. (2007).
- Thais, L. & Magnaudet, J. A triple decomposition of the fluctuating motion below laboratory wind water waves. *J. Geophys Res.* bf 100 (C1): 741-755 (1995).
- Teixeira, M.A.C. , & Belcher, S.E. On the distortion of turbulence by a progressive surface wave. *J. Fluid. Mech.*, **458**: 229–267 (2002).
- Terray, E., Donelan, M., Agrawal, Y., Drennan, W., Kahma, K., Williams, A., Hwang, P., & Kitaigorodskii, S. Estimates of kinetic energy dissipation under breaking waves. *J. Phys. Oceanog.*, **26**(5): 792–807 (1996).
- Thorpe, S. A. Energy loss by breaking waves. *J. Phys. Oceanog.*, **23**: 2498–2502 (1993).

- Thorpe, S. A. Langmuir Circulation. *Annu. Rev. Fluid Mech.*, **36**: 55–79 (2004).
- Townsend, A. A. *The structure of turbulent shear flow*. 2nd Ed. Cambridge University Press. (1976).
- Turney, D.E., Smith, W.C., & Banerjee, S. A measure of near-surface fluid motions that predicts air-water gas exchange in a wide range of conditions. *Geophys. Res. Let.*, **32**, doi:10.1029/2004GL021671 (2005).
- Veron, F., & Melville, W. K. Pulse-to-Pulse Coherent Doppler Measurements of Waves and Turbulence. *J. Atmos. Ocean. Tech.*, **16**: 1580–1597 (1999a).
- Veron, F., & Melville, W. Laboratory studies of mixing and Langmuir circulations. In M. Banner, editor, *Proc. Symp. on the Wind-Driven Air-Sea Interface*, pages 265–272. ADFA, Canberra, Univ. NSW, Sydney (1999b).
- Veron, F., & Melville, W. K. Experiments on the stability and transition of wind-driven water surfaces. *J. Fluid Mech.*, **446**: 25–65 (2001).
- Veron, F., Melville, W. K. & Lenain, L. Wave coherent heat flux. *J. Phys. Oceanogr. - In Press* (2008a)
- Veron, F., Melville, W. K. & Lenain, L. Infrared techniques for measuring ocean surface processes. *J. Ocean. Atmos. Tech. - In Press* (2008b)
- Uz, B.M., Donelan, M.A., Hara, T. & Bock, E/J. Laboratory studies of wind stress over surface waves. *Bound. Layer Meteor.*, **102**: 301–331 (2002).
- Webb, E.K., Pearman, G.I. & Leuning, R. measurements for density effects due to heat and water vapor transfer. *Quart. J. R. Meteorol. Soc.*, **106**: 85–106 (1980).
- Young I.R. (1994) On the measurement of directional spectra. *Applied Ocean Research*, **16**: 283–294 (1994)

Zappa C.J., Asher W.E., & Jessup, A.T. Microscale wave breaking and air-water gas transfer. *J. Geophys. Res.*, **106**(C5): 9385–9391 (2001).

Figure Captions

FIG. 1. (a) Instrumentation setup from *R/P FLIP*. (b) Map of the deployment area; *R/P FLIP* was moored off the coast of southern California in August 2003.

FIG. 2. (a) Wind speed (black) and direction (gray) measured with the sonic anemometer for the duration of the experiment. (b) Spectrogram of the surface elevation $S_{\eta\eta}$, measured with the laser altimeter. Note the two peaks at the frequencies of the swell and the wind waves. (c) Significant wave height measured with the altimeter and compared with that obtained from the RDI waves ADCP (\bullet).

FIG. 3. Infrared image of the surface temperature and surface turbulent velocity field calculated from the passive temperature pattern displacements between this temperature image and one taken 33 *ms* later. (a) Shows the temperature and surface velocity for a wind speed of $U_{10} = 0.5 \text{ m s}^{-1}$ with large upwelling/convection, and (b) for a wind speed of $U_{10} = 3.8 \text{ m s}^{-1}$ where cold streaks (Langmuir circulations) are clearly visible.

FIG. 4. Two-dimensional wavenumber spectra of the surface divergence (a), vorticity (b) and surface temperature (c) for a wind speed of 8 m s^{-1} . The spectra were calculated from an average of 120 individual spectra taken over one minute of data starting at 05:03 UTC on 23 Aug 2003. (d) Shows the directions for the wind, from 305° , the wind waves, to 117° , the swell, to 97° , the vorticity spectral peak, 52° , the divergence spectral peak, 122° , and the temperature spectral peak, 43° .

FIG. 5. (a) Direction of the wind, wind-waves, swell and current. (b) Directions of the streaks (i.e. the direction perpendicular to that of the peak spectral densities and the maximum variance), for the vorticity, divergence, shear, and normal deformation.

FIG. 6. Examples of streamline patterns showing hyperbolic surface velocity fields as in equation 14 where α_i , β_i , and γ_i where chosen randomly. The scale is arbitrary.

FIG. 7. Time series of surface displacement and the spatial variance of the along wave surface turbulence over a 120 s record starting at 05:00 (UTC) on August 24th, 2003.

FIG. 8. Spectragrams of (a) the surface displacement η and (b) the along wave turbulent surface velocity u'_1 , at night. (c) and (d) show the squared coherence and phase between the surface displacement and the turbulent surface velocity, respectively .

FIG. 9. Variance of the wave-coherent, along wave, surface velocity turbulence with the wind speed (a) and the rms surface wave slope (b). The large symbols show the bin-averaged data and the solid lines are the fits to the bin averaged data.

FIG. 10. Fraction of variance of the wave coherent turbulence ($\overline{\tilde{u}_1^2}$) to the total variance in the turbulence ($\overline{u_1'^2}$) as a function of the wave slope. The large symbols show the bin-averaged data and the solid gray line shows the rapid distortion theory prediction of equation 18.

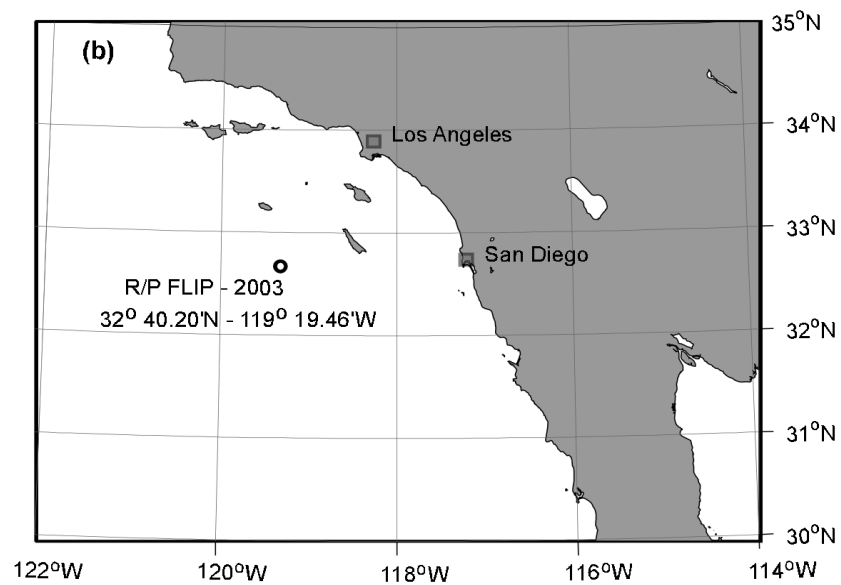
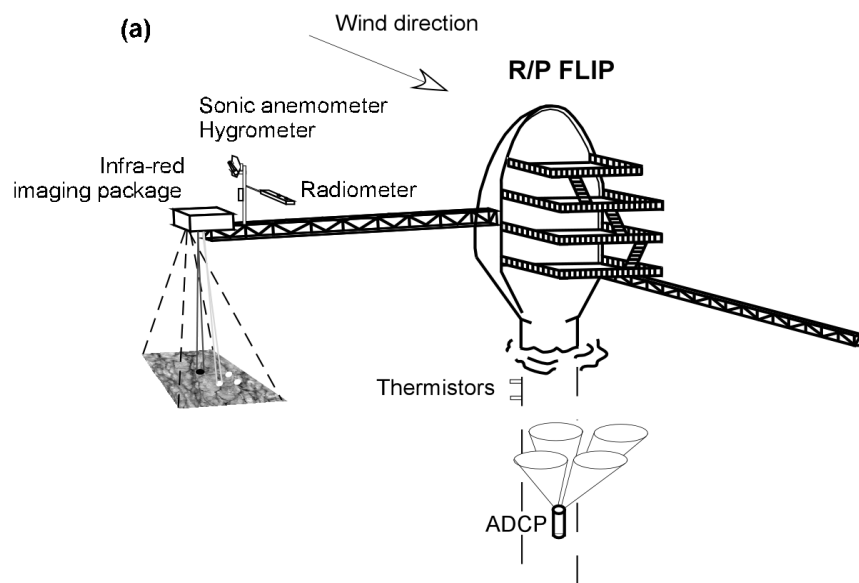


FIG. 1. (a) Instrumentation setup from *R/P FLIP*. (b) Map of the deployment area; *R/P FLIP* was moored off the coast of southern California in August 2003.

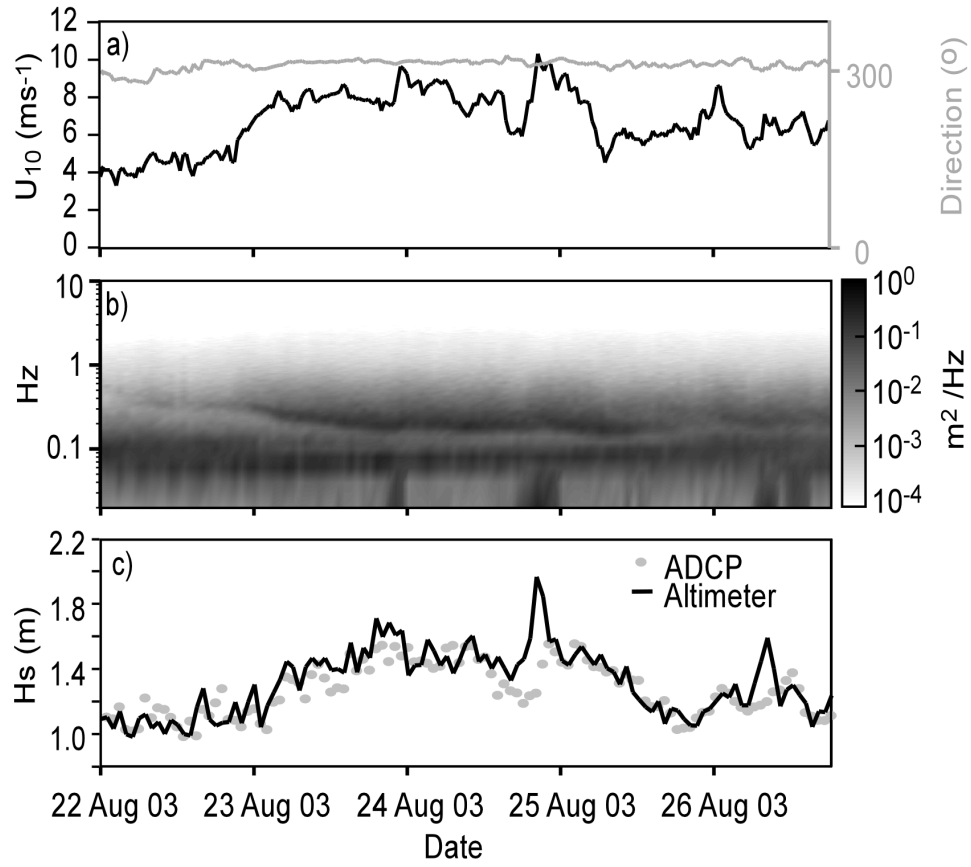


FIG. 2. (a) Wind speed (black) and direction (gray) measured with the sonic anemometer for the duration of the experiment. (b) Spectrogram of the surface elevation $S_{\eta\eta}$, measured with the laser altimeter. Note the two peaks at the frequencies of the swell and the wind waves. (c) Significant wave height measured with the altimeter and compared with that obtained from the RDI waves ADCP (•).

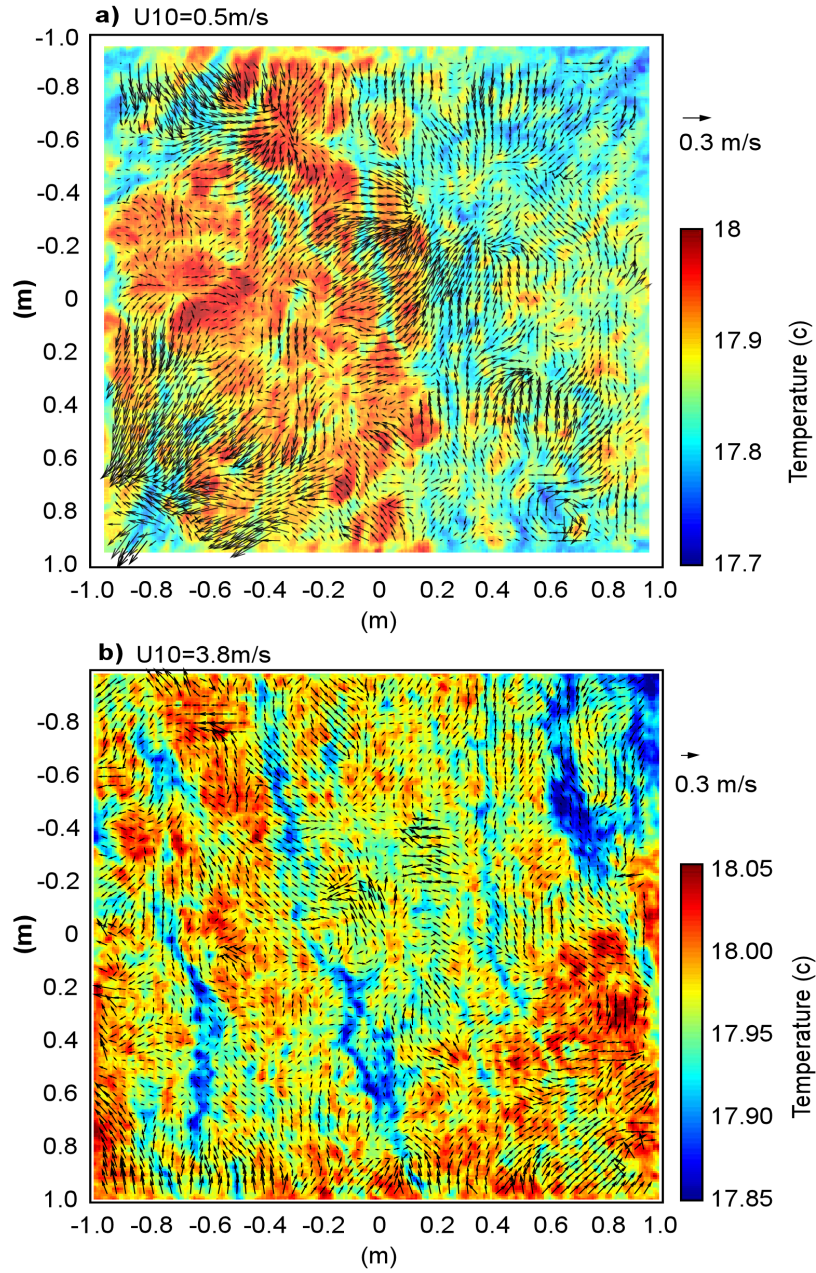


FIG. 3. Infrared image of the surface temperature and surface turbulent velocity field calculated from the passive temperature pattern displacements between this temperature image and one taken 33 ms later. (a) Shows the temperature and surface velocity for a wind speed of $U_{10} = 0.5 \text{ m s}^{-1}$ with large upwelling/convection, and (b) for a wind speed of $U_{10} = 3.8 \text{ m s}^{-1}$ where cold streaks (Langmuir circulations) are clearly visible.

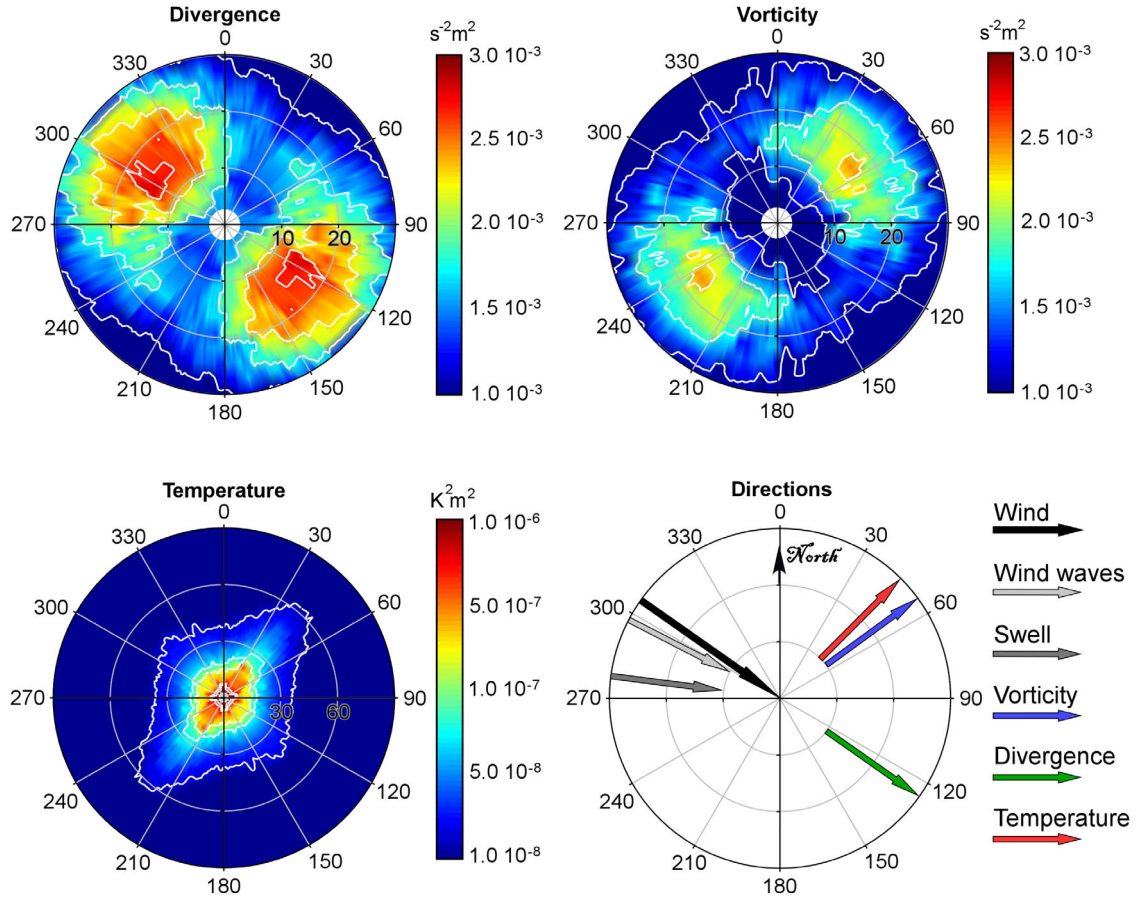


FIG. 4. Two-dimensional wavenumber spectra of the surface divergence (a), vorticity (b) and surface temperature (c) for a wind speed of 8 m s^{-1} . The spectra were calculated from an average of 120 individual spectra taken over one minute of data starting at 05:03 UTC on 23 Aug 2003. (d) Shows the directions for the wind, from 305° , the wind waves, to 117° , the swell, to 97° , the vorticity spectral peak, 52° , the divergence spectral peak, 122° , and the temperature spectral peak, 43° .

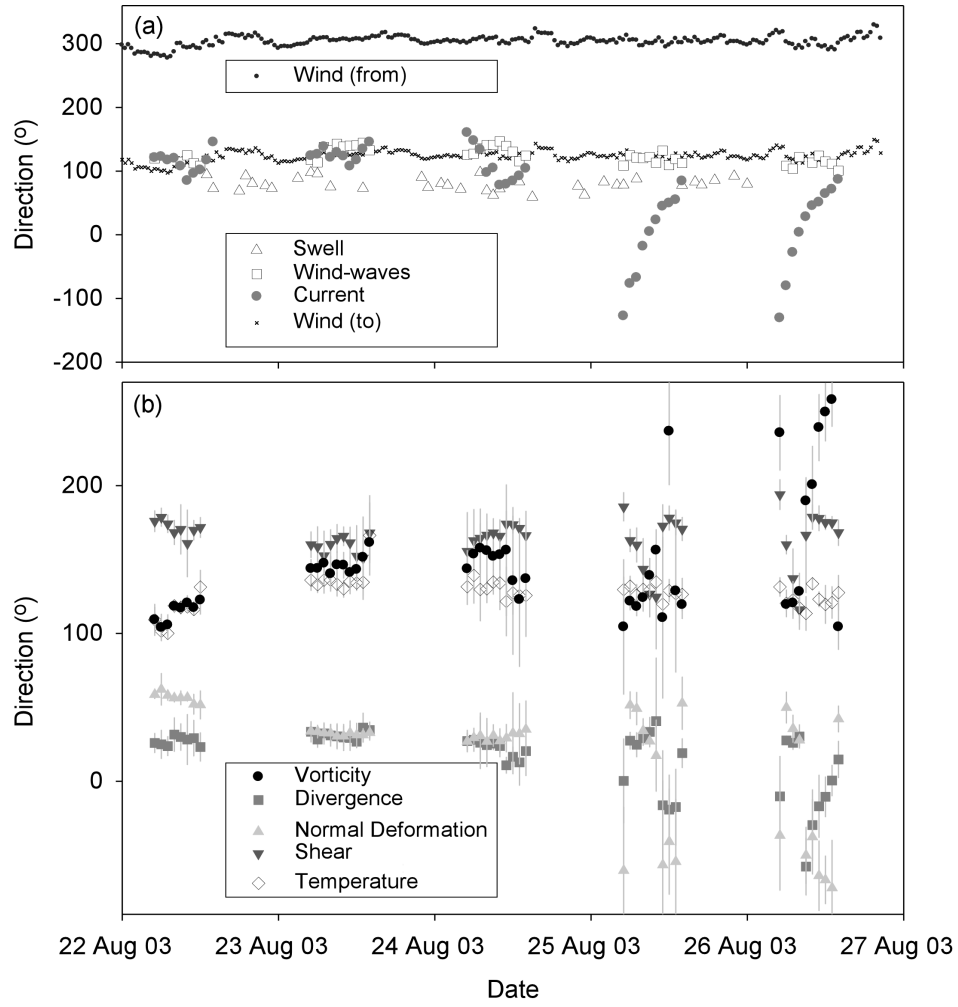


FIG. 5. (a) Direction of the wind, wind-waves, swell and current. (b) Directions of the streaks (i.e. the direction perpendicular to that of the peak spectral densities and the maximum variance), for the vorticity, divergence, shear, and normal deformation.

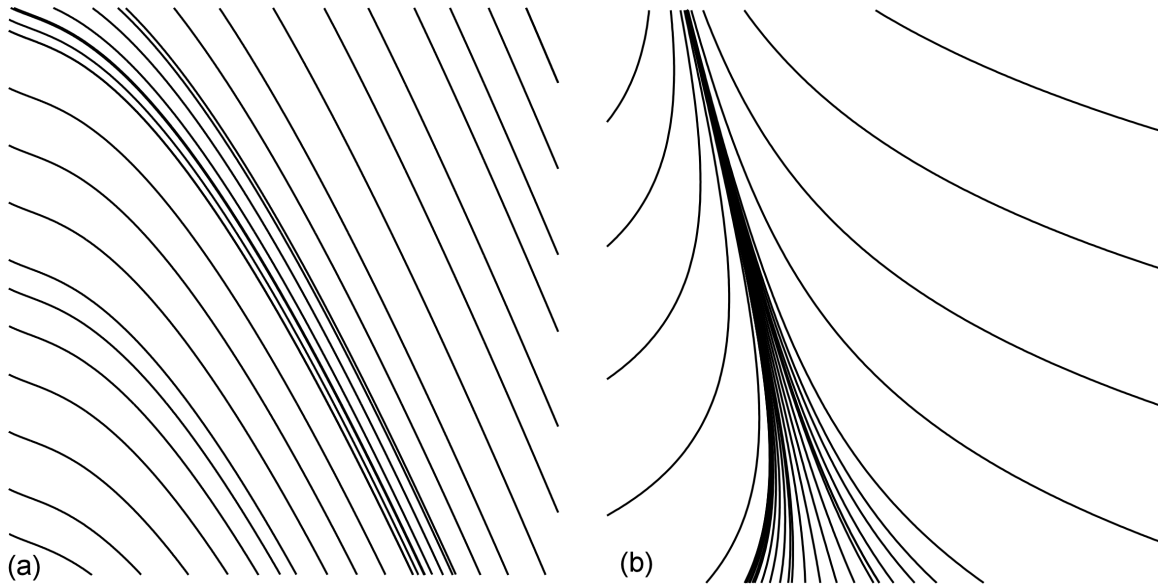


FIG. 6. Examples of streamline patterns showing hyperbolic surface velocity fields as in equation 14 where α_i , β_i , and γ_i where chosen randomly. The scale is arbitrary.

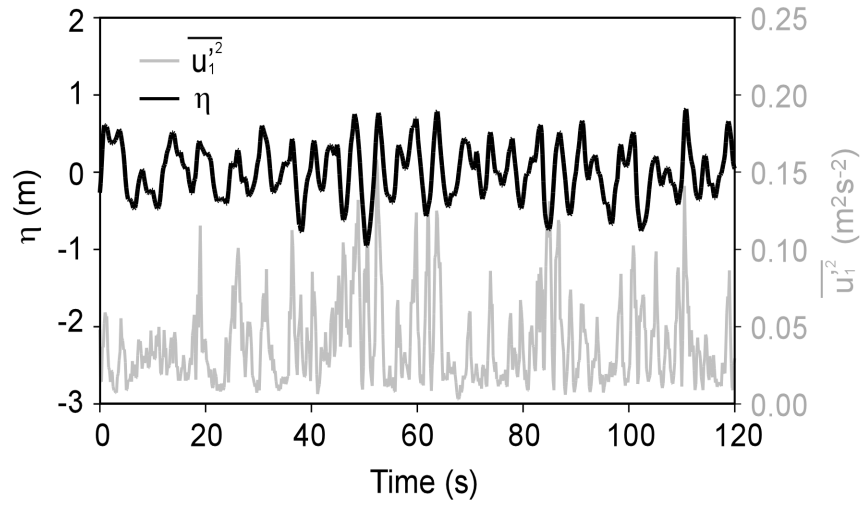


FIG. 7. Time series of surface displacement and the spatial variance of the along wave surface turbulence over a 120 *s* record starting at 05:00 (UTC) on August 24th, 2003.

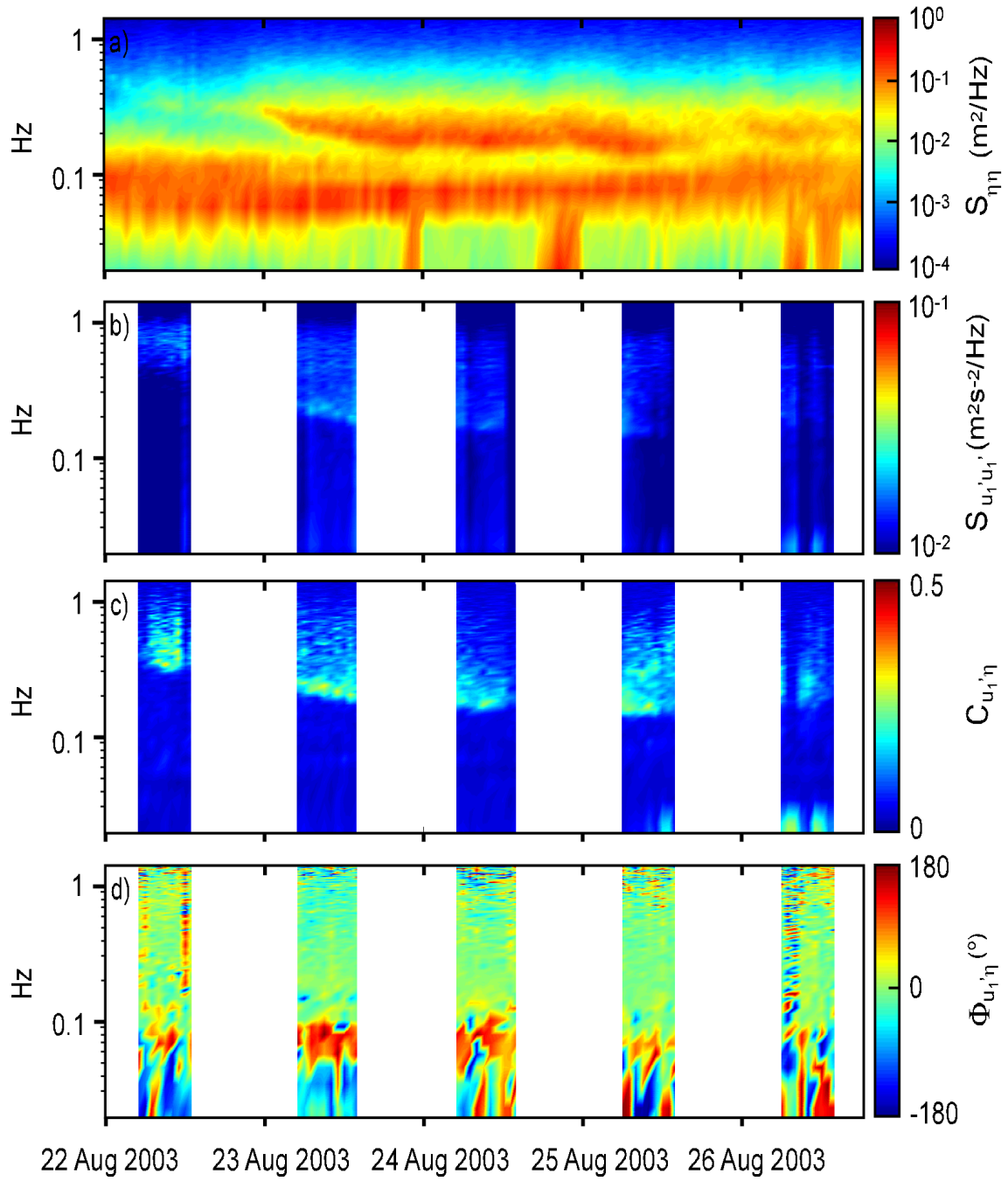


FIG. 8. Spectragrams of (a) the surface displacement η and (b) the along wave turbulent surface velocity u_1' , at night. (c) and (d) show the squared coherence and phase between the surface displacement and the turbulent surface velocity, respectively .

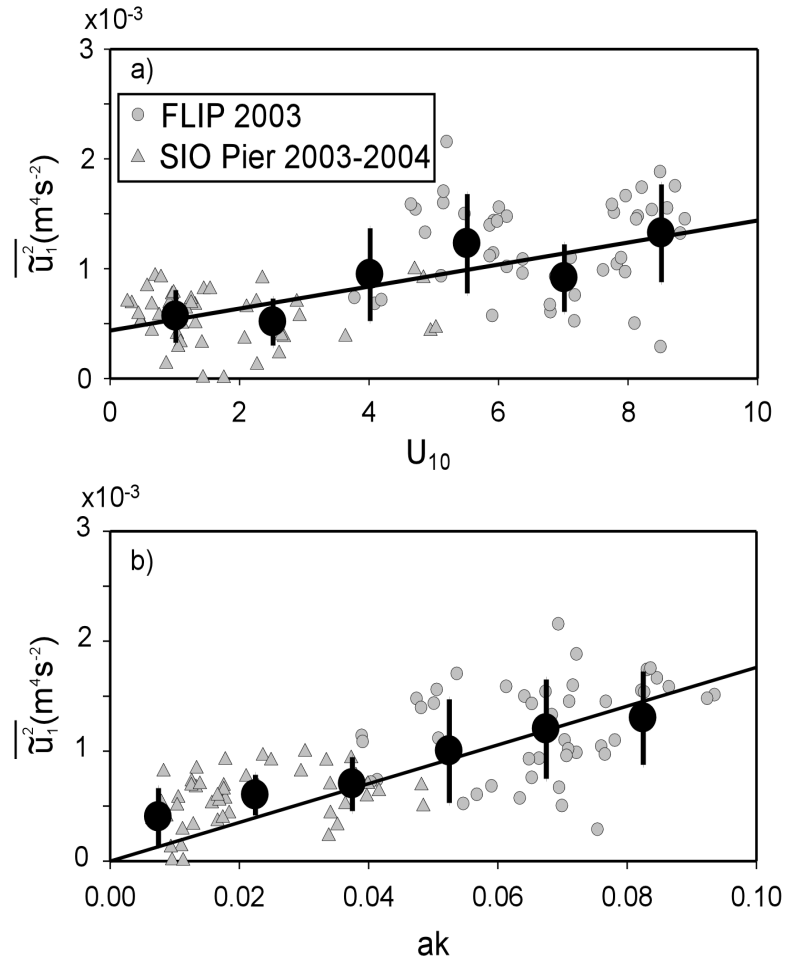


FIG. 9. Variance of the wave-coherent, along wave, surface velocity turbulence with the wind speed (a) and the rms surface wave slope (b). The large symbols show the bin-averaged data and the solid lines are the fits to the bin averaged data.

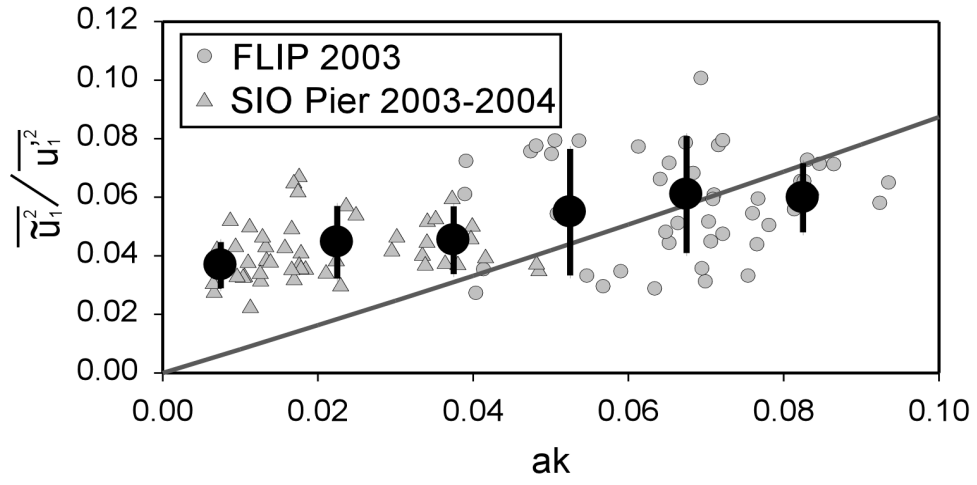


FIG. 10. Fraction of variance of the wave coherent turbulence ($\overline{\tilde{u}_1^2}$) to the total variance in the turbulence ($\overline{u_1'^2}$) as a function of the wave slope. The large symbols show the bin-averaged data and the solid gray line shows the rapid distortion theory prediction of equation 18.